Key Points:
- A sharp oceanic front has been thoroughly sampled using combined in situ and remote sensing observations
- A new method builds on directional Sun glitter reflections to quantitatively interpret the roughness changes over the front
- This multiangle roughness anomaly helps to unambiguously derive the intense deformation field at the front

Correspondence to:
N. Rascle,
nicolas.rascle@ifremer.fr

Intense deformation field at oceanic front inferred from directional sea surface roughness observations

Nicolas Rascle[1] (iD), **Jeroen Molemaker**[1] (iD), **Louis Marié**[1] (iD), **Frédéric Nouguier**[2] (iD), **Bertrand Chapron**[1], **Björn Lund**[2] (iD), and **Alexis Mouche**[1]

[1] Laboratoire d'Océanographie Physique et Spatiale (LOPS), IUEM, University Brest, CNRS, IRD, Ifremer, Brest, France, [2] Department of Ocean Sciences, Rosenstiel School of Marine and Atmospheric Science, University of Miami, Miami, Florida, USA

Abstract Fine-scale current gradients at the ocean surface can be observed by sea surface roughness. More specifically, directional surface roughness anomalies are related to the different horizontal current gradient components. This paper reports results from a dedicated experiment during the Lagrangian Submesoscale Experiment (LASER) drifter deployment. A very sharp front, 50 m wide, is detected simultaneously in drifter trajectories, sea surface temperature, and sea surface roughness. A new observational method is applied, using Sun glitter reflections during multiple airplane passes to reconstruct the multiangle roughness anomaly. This multiangle anomaly is consistent with wave-current interactions over a front, including both cross-front convergence and along-front shear with cyclonic vorticity. Qualitatively, results agree with drifters and X-band radar observations. Quantitatively, the sharpness of roughness anomaly suggests intense current gradients, 0.3 m s^{-1} over the 50 m wide front. This work opens new perspectives for monitoring intense oceanic fronts using drones or satellite constellations.

1. Introduction

Surface roughness images often capture spectacular manifestations of fine-scale upper ocean dynamics, including intense fronts and filaments at scales down to less than 100 m [e.g., *Fu and Holt*, 1983; *Alpers*, 1985; *Yoder et al.*, 1994]. Those images are routinely obtained with high-resolution satellite sensors, e.g., from passive optical radiometers viewing areas in and around the Sun glitter [e.g., *Scully-Power*, 1986; *Rascle et al.*, 2016] and from active radar instruments like synthetic aperture radars (SARs) [e.g., *Apel et al.*, 1975; *Beal et al.*, 1981; *Kudryavtsev et al.*, 2012a]. In the near future, the multiplication of nanosatellites and drones could provide new means to monitor those intense fine-scale structures.

Fine-scale features observed on surface roughness images relate to the modulations of short (wavelength ~1 m) wind waves by horizontal current gradients [*Phillips*, 1984; *Dulov and Kudryavtsev*, 1990; *Rascle et al.*, 2014]. Different components of the horizontal current gradient can impact different directional properties of surface roughness [*Rascle et al.*, 2016]. In particular, an isotropic divergence of the current has a perfect directional symmetry, resulting in surface roughness anomalies independent on azimuthal view direction. At variance, anisotropic components of the current gradient, like vorticity or strain, create anisotropic surface roughness anomalies. This is illustrated in Figure 1. The background (i.e., unperturbed by current) wind waves are supposed to have a nearly Gaussian slope distribution, with $P_0(z_x, z_y)$ the probability density function (PDF) of eastward z_x and northward z_y slopes. An isotropic current divergence creates an anomalous slope distribution $P = P_0 + P'$ with quasi-circular contrast P'/P compared to the background. On the contrary, an anisotropic current gradient, e.g., a current strain, creates an anisotropic distribution of slopes contrast.

To further dwell on these directional properties, a dedicated experiment was conducted during LASER (Lagrangian Submesoscale Experiment), where hundreds of drifters were deployed. A very sharp front, 50 m wide, was detected simultaneously in drifter trajectories, sea surface temperature, and sea surface roughness (section 2). Using Sun glitter reflections during multiple airplane passes, the multiangle roughness anomaly can be precisely reconstructed. Compared to a satellite which can only perform one pass over the front, thus providing a maximum of two azimuths view angles at a given zenith angle [e.g., *Rascle et al.*, 2016],
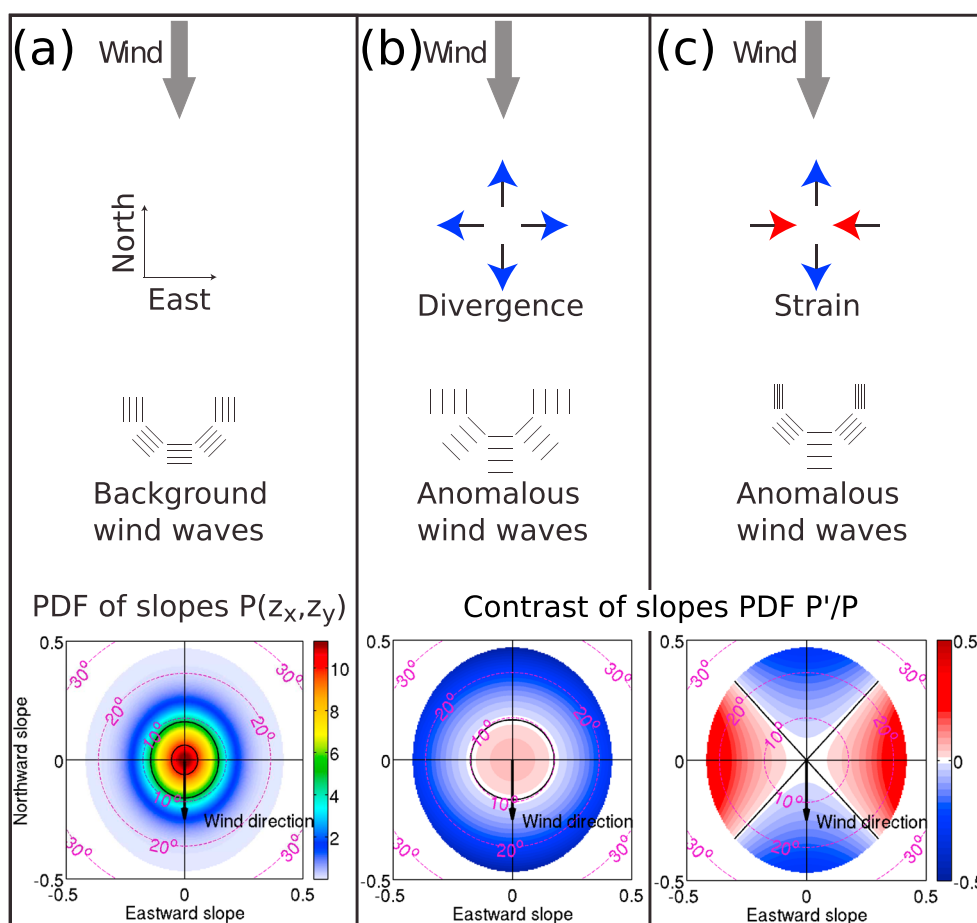
Figure 1. (a) Sketch of the background wind waves and the PDF $P(z_x, z_y)$ of eastward and northward slopes. (b and c) Wind wave in the presence of current divergence or strain, and associated PDF contrast P'/P.

the airplane performs multiple passes, providing the surface roughness anomaly at many different azimuth angles. The surface roughness clearly presents anisotropic anomalies (section 3). This anisotropy cannot be explained by surfactants nor by an isotropic current convergence. It is consistent with a front with cross-frontal convergence plus along-front current shear (section 4). As obtained, the surface roughness anomaly is very sharp, suggesting current gradient of the order of 40 f, with the Coriolis frequency f, over a front width of 30 to 50 m. The deployed drifters and X-band radar measurements provide qualitatively consistent estimates of current gradients at scales about 500 m. Quantitatively, surface roughness suggests a much sharper front with current gradients an order of magnitude larger (section 5).

2. The Experiment

2.1. The LASER Drifter Deployment
Data were obtained on 11 February 2016 during the Lagrangian Submesoscale Experiment (LASER), where a large number ($O(1000)$) of surface drifters were deployed within the Gulf of Mexico (Figure 2a). The wind was blowing from the WSW (255°) about 9 m s^{-1}, as revealed from nearby meteorological buoys (National Data Buoy Center station 42040). About 180 drifters got caught into an oceanic front with a sharp sea surface temperature (SST) jump of about $0.5-0.7°$C over 50 m (Figure 2b). An airplane (Partenavia P.68) was used to fly over the front at about 1000 m altitude, acquiring SST using an infrared camera and surface roughness using visible cameras looking at the Sun glint.

2.2. The Visible Cameras
The visible light intensity was measured by two panchromatic cameras (JAI BM-500GE) equipped with a 5 mm focal length low distortion lens to ensure a large field of view. The cameras setup is sketched in Figure 3a.
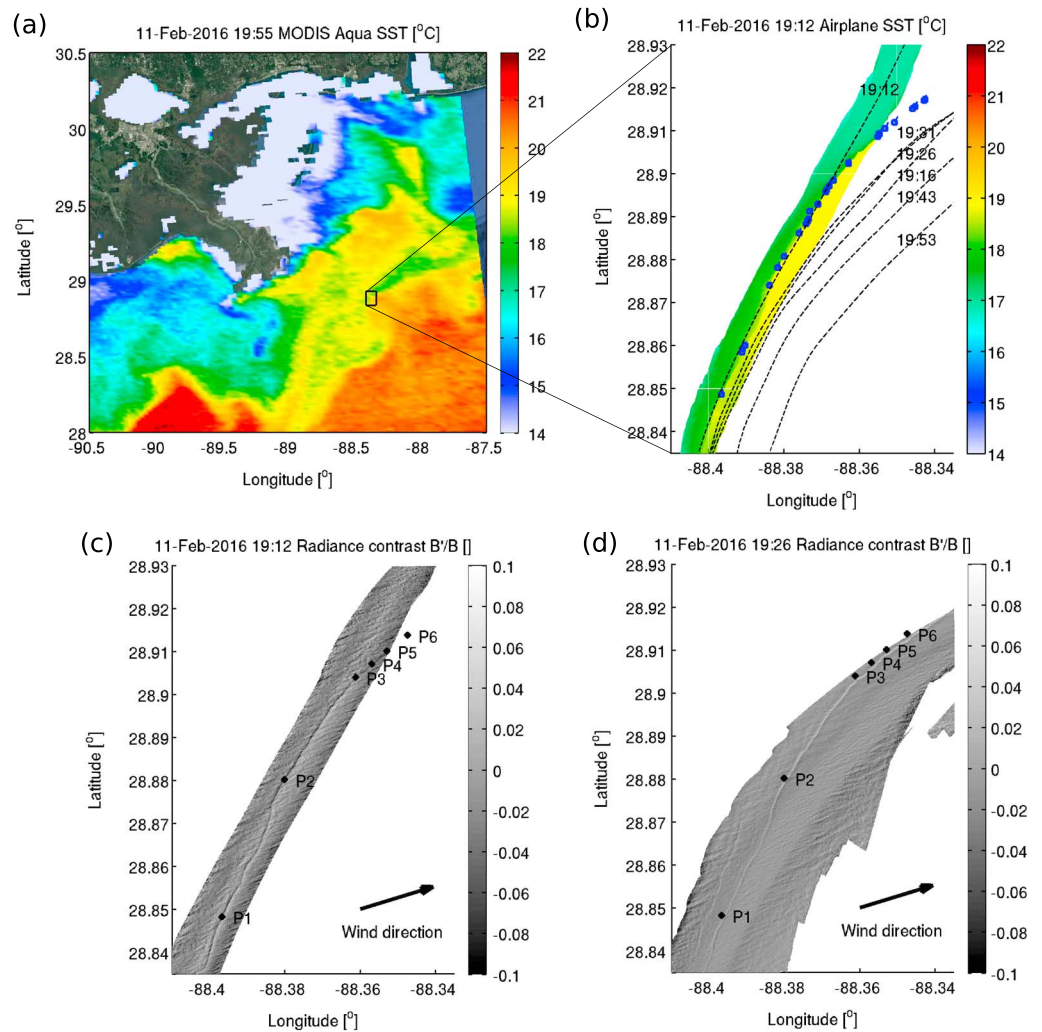
Figure 2. (a) SST from Moderate Resolution Imaging Spectroradiometer (MODIS) [*Salomonson et al.*, 1989] on board *Aqua*. (b) SST composite from the first airplane overpass at 19:12 UTC. The LASER drifters are shown in blue, and the ground tracks of the six airplane passes are shown in dashed lines. (c) Composite of radiance contrast B'/B at facet angles inside the ellipse of Figure 4f, for the first airplane overpass at 19:12 UTC. (d) Composite for angles outside the ellipse, for the third airplane overpass at 19:26 UTC. In Figure 2c and 2d, the 6 points used for the surface roughness analysis are shown in black.

The two cameras are arranged symmetrically about the airplane nadir with a pitch of $\pm 35°$ for the forward/aftward cameras. The camera aperture angles are $80° \times 70°$ along track and across track, respectively, with 2456×2058 pixels in the respective directions. For a flight altitude of 1000 m, this leads to a ground resolution from 0.5 to 6 m. The cameras acquired images at 2 Hz. The images are geolocated using an internal motion unit (Applanix POS AV V610).

2.3. Sun Glint and Geometry

We consider the surface brightness field in the Sun glitter area where the impact of the sky radiance reflected from the surface to the sensor is negligible. Following *Cox and Munk* [1954], the Sun glitter radiance, *B*, generated by specular reflection of the sunlight is given as

$$B = \frac{\rho E_s}{4 \cos \theta_c \cos^4 \theta_f} P \left(z_{xf}, z_{yf} \right) . \tag{1}$$

In this expression, E_s is the Sun irradiance, ρ is the Fresnel reflection coefficient, $P(z_x, z_y)$ is the 2-D probability density function (PDF) of the eastward (z_x) and northward (z_y) sea surface slopes, and z_{xf} and z_{yf} are the slopes of the surface facet satisfying the conditions of specular reflection of the sunlight toward the camera.
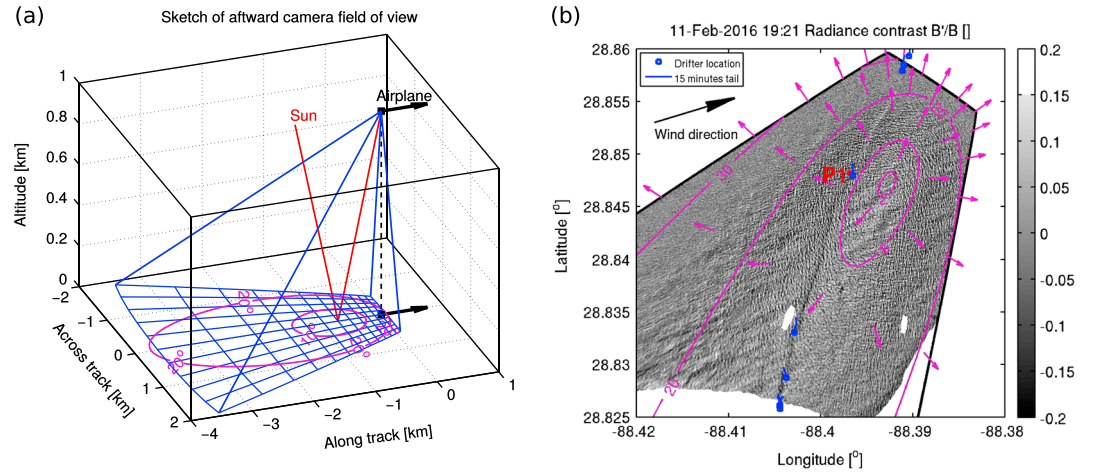
Figure 3. (a) Sketch of the field of view of the aftward camera, for a flight altitude of 1000 m. The varying horizontal resolution is shown with each rectangle representing 200 × 200 pixels. Here we show the special case of the Sun exactly at the rear of the airplane and with a zenith angle of 35°. In such case the specular sunspot is at the center of the camera field of view, and pink contours indicate the zenith angle θ_f of surface facets reflecting the Sun. (b) Example of one image of radiance contrast B'/B, at 19:16 UTC, around point P1. Eight drifters (in blue) are caught along the front. Pink contours and arrows indicate respectively the zenith and azimuth angles of the facets reflecting the Sun.

The slopes of the specular facet are

$$z_{xf} = -\frac{\sin\theta_s \sin\varphi_s + \sin\theta_c \sin\varphi_c}{\cos\theta_s + \cos\theta_c}, z_{yf} = -\frac{\sin\theta_s \cos\varphi_s + \sin\theta_c \cos\varphi_c}{\cos\theta_s + \cos\theta_c}, \quad (2)$$

where θ_c and θ_s are the camera and Sun zenith incidence angles (measured from the vertical) and φ_c and φ_s the camera and Sun azimuth angles (measured clockwise from north). Finally, the zenith and azimuth angles of the specular facet are

$$\theta_f = \arctan\sqrt{z_{xf}^2 + z_{yf}^2}, \quad \varphi_f = \arctan(z_{yf}/z_{xf}). \quad (3)$$

2.4. Radiance Contrasts

The observed intensity $B = B_0 + B'$ is separated between a slowly varying background B_0 (mainly due to varying viewing geometry) and a local anomaly B' (due to wave-current interactions). Because of the low flight altitude of 1000 m, the cutoff scale L is set to 200 m such that at scales below L, the geometry of the observation can be considered constant. Then from (1) one has

$$\frac{B'}{B} = \frac{P'}{P}, \quad (4)$$

i.e., local radiance contrasts are due to slopes PDF contrasts induced by wave-current interactions [*Kudryavtsev et al.*, 2012b].

3. Multi-angle Radiance Contrast Over the Front

The radiance contrast B'/B at the front is measured for different viewing geometries, i.e., at different specular facet angles (z_{xf}, z_{yf}).

A snapshot of radiance contrast at the front is shown in Figure 3b. We first focus on point P1 within the front (Figures 2 and 3) and compute the radiance contrast compared to neighboring values outside of the front. Each airplane pass provides a set of observations of P1 at different viewing geometries, more specifically along a line on the slope plane (z_{xf}, z_{yf}) (Figure 4a). As the six airplane passes followed slightly different tracks, they provide six different lines of observations on the slope plane (z_{xf}, z_{yf}). Of special interest is the 19:16 pass. It provides in particular two observations at similar zenith angles of $\theta_f \simeq 15°$ but different azimuths φ_f. The radiance contrast at the front is negative for upwind viewing geometry whereas it is positive for crosswind view. Such azimuthal contrast inversion has already been noted from multilook satellite images
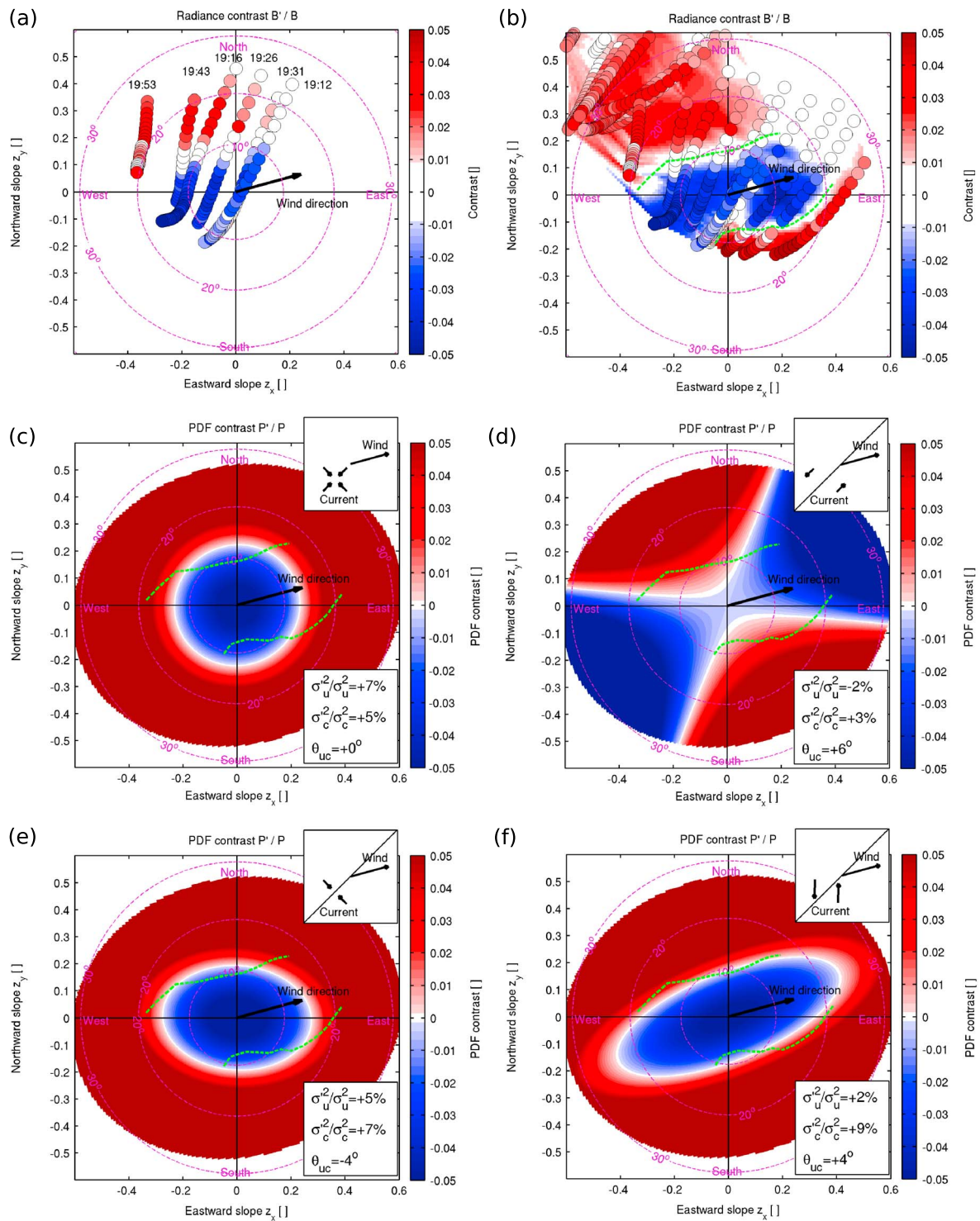
Figure 4. (a and b) Observed radiance contrasts for (a) the six passes over point P1 and (b) with the additional passes over points P2 to P6. The green dotted line highlights the location of contrast inversion. (c to f) Model PDF contrasts for (c) isotropic convergence, (d) along-front current with shear, (e) across-front current with convergence, and (f) current as a linear combination 1.2(d) + 0.8(e). The wind is set to 9 m s^{-1} from the WSW (255°) and the front orientation is set to SW-NE (45°).

by *Rascle et al.* [2016], for the much wider ($\sim$5 km) front of the Gulf Stream. As satellites only pass once over a region, they do not provide more than two different azimuths at a given zenith view angle. On the contrary, the present airplane measurements provide a much more complete view of the surface roughness anomaly, with up to 10 different azimuth views at a constant zenith angle of 12°.

Additional viewing angles can be obtained if one supposes that the current and surface roughness are uniform in the along-front direction. For instance, the 19:12 track crosses the front north of point P1, around points P3 to P6 (Figure 2), which provides different view angles. Figure 4b cumulates the different passes over the points P1 to P6, giving a more complete description of the radiance contrast at the front. It enables an estimated location of the contrast inversion (Figure 4b, green dotted line), which is clearly elongated along the wind direction. Such multiangle surface roughness anomalies have not been reported before.

4. Interpretation in Terms of Current Gradient

We hypothesize that wave-current interactions are responsible for surface roughness anomaly. We ignore the impact of surfactants [e.g., *Espedal et al.*, 1998; *McWilliams et al.*, 2009], mostly limited to lower wind speeds. We also ignore atmospheric boundary layer modifications [e.g., *Beal et al.*, 1997], which seemingly occurs at larger spatial scales [*Kudryavtsev et al.*, 2005].

To investigate short wave transformation, we run the model of short waves of *Kudryavtsev et al.* [2005], in its simplified configuration which neglects propagation as described in *Johannessen et al.* [2005]. The model calculates the evolution of the spectrum of wave action $N(\mathbf{x}, \mathbf{k})$ (in $m^5 \ s^{-1}$), where $\mathbf{x} = (x, y)$ is the horizontal position and $\mathbf{k} = (k_x, k_y)$ the wave number. Following a relaxation approach [e.g., *Keller and Wright*, 1975; *Hughes*, 1978; *Alpers and Hennings*, 1984], the action is written $N(\mathbf{x}, \mathbf{k}) = N_0(\mathbf{k}) + N'(\mathbf{x}, \mathbf{k})$ where N' represents small disturbance with respect to a background value N_0 corresponding to the state undisturbed by currents. The anomaly N' due to local current variations reads

$$N'(\mathbf{x}, \mathbf{k}) = \tau_c \begin{bmatrix} k_x & k_y \end{bmatrix} \begin{bmatrix} \frac{\partial u}{\partial x} & \frac{\partial u}{\partial y} \\ \frac{\partial v}{\partial x} & \frac{\partial v}{\partial y} \end{bmatrix} \begin{bmatrix} \frac{\partial N_0}{\partial k_x} \\ \frac{\partial N_0}{\partial k_y} \end{bmatrix} \tag{5}$$

where $\tau_c(\mathbf{k})$ is a relaxation time scale and (u, v) are the horizontal components of the surface current.

The second moments of the wave spectrum are the upwind m_u, crosswind m_c, and cross-correlated m_{uc} mean square slopes (mss), defined by

$$m_u(\mathbf{x}) = \int \int_{\mathbf{k}} \omega^{-1} k N \quad k_x^2 \quad \mathbf{dk},$$

$$m_c(\mathbf{x}) = \int \int_{\mathbf{k}} \omega^{-1} k N \quad k_y^2 \quad \mathbf{dk}, \tag{6}$$

$$m_{uc}(\mathbf{x}) = \int \int_{\mathbf{k}} \omega^{-1} k N \quad k_x k_y \quad \mathbf{dk},$$

where ω is the intrinsic frequency and without loss of generality we have set here the x axis in the wind direction.

The PDF of surface slopes is supposed Gaussian and reads [*Longuet-Higgins*, 1957]

$$P(z_x, z_y) = \frac{1}{2\pi\Delta^{1/2}} \exp - \left(\frac{z_x^2 m_c + z_x z_y m_{uc} + z_y^2 m_u}{2\Delta} \right), \tag{7}$$

where $\Delta = m_u m_c - m_{uc}^2$, and where the angle of the principal axis is given by $\tan 2\theta_{uc} = 2m_{uc}/(m_u - m_c)$.

The wind is set to 9 m s^{-1} from the WSW (255°), and the front orientation is set to SW-NE (45°). We first focus on the sign of the surface roughness anomaly, before considering its magnitude.

4.1. Sign of the Current Gradient

In the first model run, the current is set to an isotropic convergence (Figure 4c), with a perfect directional symmetry. As illustrated in Figure 1b, waves propagating in any direction experience a compression by the current gradient, increasing the mss in all directions ($m'_u > 0, m'_c > 0$). The PDF contrast P'/P is then nearly isotropic, with a contrast inversion occurring at a zenith angle about $\theta_m \simeq \arctan(\sqrt{2m_u}) \simeq 13°$. Such isotropic

PDF contrast would be similar to that produced by surfactants and reported, e.g., by *Cox and Munk* [1954]. The clear anisotropy of our observed radiance contrast points toward anisotropic current gradients.

Following our hypothesis of along-front homogeneity, the current gradients could be a combination of along-front current shear and across-front current divergence. The case of along-front current shear with positive vorticity is shown in Figure 4d. As the wind blows obliquely to the front, it creates a positive strain in the wind direction(To understand this decomposition, see, e.g., Figure 6 in *Rascle et al.* [2016]) which elongates the waves in the wind direction ($m'_u < 0$) and compresses the waves in the crosswind direction ($m'_c > 0$), as illustrated in Figure 1c. The resulting slope PDF is thus separated into four quadrants. The signs of the observed radiance contrast indicates current with positive vorticity, as negative vorticity would produce quadrants of reversed signs.

The case of across-front current convergence is shown in Figure 4e. It is qualitatively similar to the case of isotropic convergence (Figure 4c), except that crosswind waves are slightly more compressed than along-wind waves. As a result, the zone of PDF contrast inversion is no longer nearly circular but elongated in the wind direction. The sign of the observed contrast indicates current with positive convergence.

In all cases above, there is a discrepancy between model and observations in terms of the position of the contrast inversion (green dotted line). A correct position of the contrast inversion can be obtained with a combination of positive vorticity plus positive across-front convergence. Good agreement is obtained for a ratio of along-front shear to across-front convergence of the order of 1 to 3, with 1.5 being our best fit (Figure 4f).

Composite images of radiance contrasts B'/B were created for each airplane pass (Figures 2d and 2e). Observations were separated according to whether the view angle (z_{xf}, z_{yf}) is inside (Figure 2d) or outside (Figure 2e) the ellipse of contrast inversion shown in Figure 4f. Consistently with our analysis, the front appears with a negative and positive roughness contrast, respectively.

4.2. Amplitude of the Current Gradient

As well established [e.g., *Phillips*, 1984], the amplitude of surface roughness contrast is related to wind speed U_{10}, amplitude of current gradient du/dx and spatial extent of current gradient L_u [see *Kudryavtsev et al.*, 2012b, equation (4)],

$$\frac{\text{mss}'}{\text{mss}} \sim U_{10}^{-1} l_c^{1/2} L_u^{1/2} \frac{du}{dx}, \tag{8}$$

where l_c a fixed length scale. Our airplane measurements are limited to scales less than $L = 200$ m. Radiance contrasts of the order of 10 to 20% over 50 m are observed at the front. To produce such contrasts with a wind speed of 9 m s^{-1}, the model of *Kudryavtsev et al.* [2005] necessitates very sharp current variations, of the order of 0.1 m s^{-1} over $L_u = 30$ m (which corresponds to current gradients of $du/dx \simeq 45\,f$, with f being the Coriolis parameter) or of the order of 0.3 m s^{-1} over $L_u = 50$ m (corresponding to $du/dx \simeq 80\,f$). Larger values of L_u would not produce the sharp roughness anomalies observed.

The physical reason for such large current gradient is as follows: at 9 m s^{-1} wind speed, short waves (wavelength about 0.5 m) have a weak response to currents because they have a very short relaxation time scale τ_c (see equation (5)), which is well constrained by the wind wave growth term [*Plant*, 1982]. At fine spatial scales, those short waves nonetheless dominate mss anomalies [see *Kudryavtsev et al.*, 2012b, equation (2)] because longer waves have a too large relaxation distance $c_g \tau_c$. Current gradients estimates from radar backscatter are known to be sensitive to the coupling between short waves and longer waves more easily perturbed by currents [e.g., *Lyzenga*, 1998; *Thompson and Gasparovic*, 1986]. The present estimates from optical backscatter are less sensitive to such coupling, which is nevertheless included in the calculations [*Kudryavtsev et al.*, 2005].

5. Current Observations and Dynamical Predictions

About 180 drifters were deployed in the area during this stage of the LASER experiment. Most of them ended up aligned within the front, which suggests convergence. The trajectory of a few drifters released in the vicinity of the front suggests positive vorticity. Also, theoretical studies [*Munk et al.*, 2000], numerical simulations [*Eldevik and Dysthe*, 2002; *Roullet and Klein*, 2010], and observations [*Shcherbina et al.*, 2013] support that cyclonic vorticity is favored around oceanic fronts, because intense anticyclonic vorticity is subject to instabilities. Those indicate that the current gradient at the front was most likely an across-front convergence
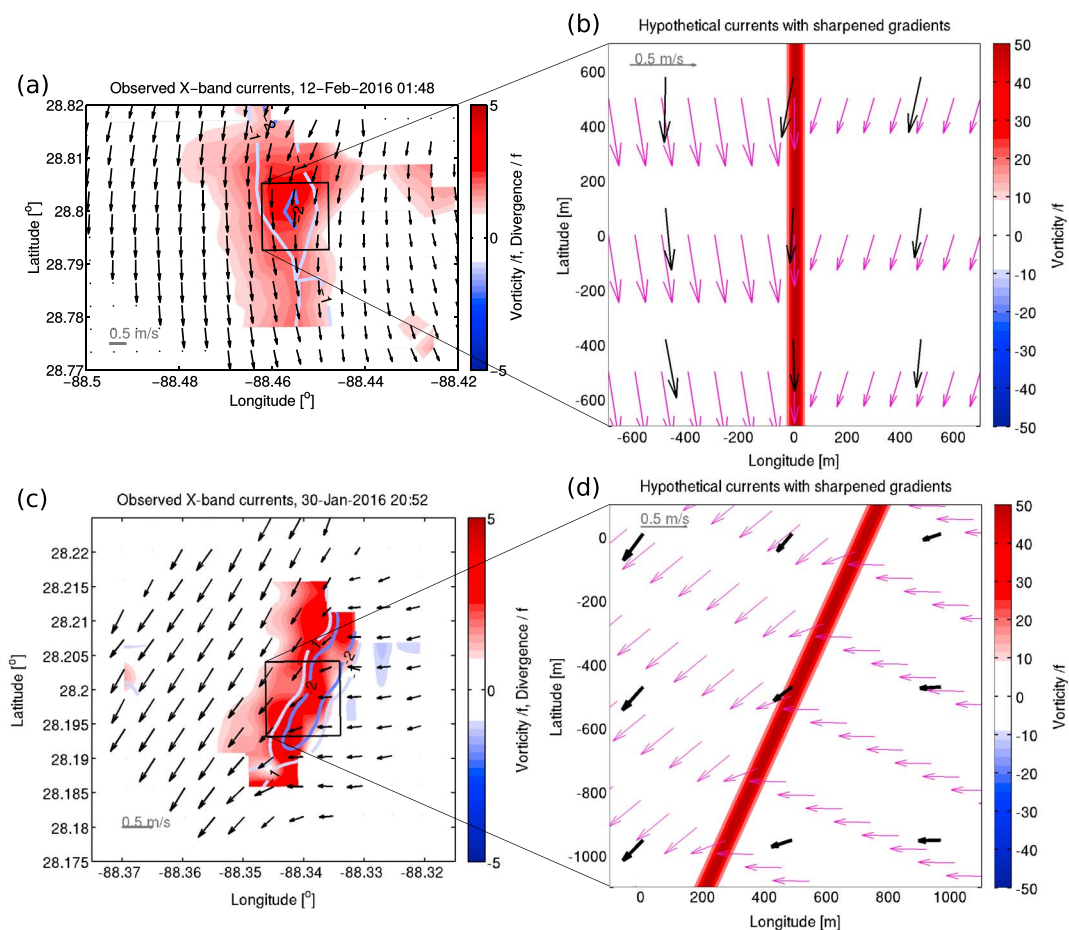
Figure 5. (a) Currents at 500 m resolution observed by X-band radar on 12 February at 01:48 UTC. Contours show divergence and colors show vorticity, both scaled by f. (b) Zoom over the area outlined in black illustrating hypothetical finer scale currents which would match the sharp current gradients estimated from surface roughness observations on 11 February at 19:30 UTC. Purple arrows are the hypothetical currents, and black arrows are the X-band observations. (c and d) Similar but for another front in the area observed on 30 January.

and/or an along-front shear with positive vorticity, in qualitative agreement with the slope PDF observed and predicted by the wave model.

Current observations were obtained 7 h later using X-band radar on board R/V *Walton Smith* [*Lund et al.*, 2015]. Those currents were retrieved at 500 m resolution and indicate as expected combinations of across-front convergence and along-front shear with positive vorticity (Figure 5a). Current variations about 20 cm s^{-1} are measured between consecutive grid points, leading to gradients about du/d$x \simeq 5$ f. The present study suggests that those current variations occur at spatial scales an order of magnitude smaller. A qualitative sketch is presented in Figure 5b. Seven hours after the airplane pass, the front was starting to weaken and become less organized. Another intense front was captured a few days earlier (30 January) in the same area and exhibits horizontal current gradients qualitatively and quantitatively compatible with the roughness observations of 11 February (Figures 5c and 5b).

To note, the present current gradients estimations are in line with the cyclonic filament measured by *Flament and Armi* [2000], who reported positive vorticity of 3 f and convergence of 0.5 f at 2 km resolution and suggested gradients greater than 7.5 f at higher (80 m) resolution.

6. Conclusion

A dedicated airborne study has been conducted to observe surface roughness anomaly induced by an oceanic front. A new method has been applied, where Sun glitter reflections during multiple airplane passes are used

to reconstruct the multiangle roughness anomaly. The anomaly is clearly anisotropic, with an inversion zone elongated along the wind direction. It confirms satellite observations of anisotropic surface roughness [*Rascle et al.*, 2016], and thanks to the airplane ability to perform multiple passes, it provides a quasi complete angular description.

The surface roughness anomaly is related to wave-current interactions. It was expected that in addition to isotropic current divergence, other anisotropic components of the current, in particular strain in the wind direction [*Rascle et al.*, 2014], should produce surface roughness anomaly. The observed multiangle anomaly is consistent with anisotropic current gradients, with across-front positive convergence plus along-front shear with a cyclonic vorticity. Those currents are qualitatively consistent with drifter observations and dynamical predictions.

As observed, the front was very sharp, 50 m wide in surface roughness and sea surface temperature. Surface roughness anomalies suggest intense current gradient, of the order of 0.3 m s^{-1} over 50 m, i.e., about 80 f. X-band radar currents provide consistent estimates of velocity jumps, but at lower horizontal resolutions.

This method of measurement confirms that oceanic fronts might be precisely characterized through their multiangle surface roughness signature. It advocates for the development of high-resolution measurements of surface roughness at multiple angles to study intense fine-scale ocean dynamics.

References

Alpers, W. (1985), Theory of radar imaging of internal waves, *Nature*, *314*(6008), 245–247.

Alpers, W., and I. Hennings (1984), A theory of the imaging mechanism of underwater bottom topography by real and synthetic aperture radar, *J. Geophys. Res.*, *89*(C6), 10,529–10,546.

Apel, J. R., H. M. Byrne, J. R. Proni, and R. L. Charnell (1975), Observations of oceanic internal and surface waves from the Earth Resources Technology Satellite, *J. Geophys. Res.*, *80*(6), 865–881.

Beal, R., V. Kudryavtsev, D. Thompson, S. Grodsky, D. Tilley, V. Dulov, and H. Graber (1997), The influence of the marine atmospheric boundary layer on ERS 1 synthetic aperture radar imagery of the Gulf Stream, *J. Geophys. Res.*, *102*(C3), 5799–5814.

Beal, R. C., P. S. DeLeonibus, and I. Katz (1981), *Spaceborne Synthetic Aperture Radar for Oceanography*, vol. 7, Johns Hopkins Univ. Press, Baltimore, Md.

Cox, C., and W. Munk (1954), Measurement of the roughness of the sea surface from photographs of the Sun's glitter, *J. Opt. Soc. Am.*, *44*(11), 838–850.

Dulov, V., and V. Kudryavtsev (1990), Imagery of the inhomogeneities of currents on the ocean surface state, *Sov. J. Phys. Oceanogr.*, *1*(5), 325–336, doi:10.1007/BF02196830.

Eldevik, T., and K. B. Dysthe (2002), Spiral eddies, *J. Phys. Oceanogr.*, *32*(3), 851–869.

Espedal, H. A., O. M. Johannessen, J. A. Johannessen, E. Dano, D. Lyzenga, and J. Knulst (1998), COASTWATCH'95: ERS 1/2 SAR detection of natural film on the ocean surface, *J. Geophys. Res.*, *103*(C11), 24,969–24,982.

Flament, P., and L. Armi (2000), The shear, convergence, and thermohaline structure of a front, *J. Phys. Oceanogr.*, *30*(1), 51–66.

Fu, L.-L., and B. Holt (1983), Some examples of detection of oceanic mesoscale eddies by the SEASAT synthetic-aperture radar, *J. Geophys. Res.*, *88*(C3), 1844–1852.

Hughes, B. (1978), The effect of internal waves on surface wind waves 2. Theoretical analysis, *J. Geophys. Res.*, *83*(C1), 455–465.

Johannessen, J., V. Kudryavtsev, D. Akimov, T. Eldevik, N. Winther, and B. Chapron (2005), On radar imaging of current features: 2. Mesoscale eddy and current front detection, *J. Geophys. Res.*, *110*, C07017, doi:10.1029/2004JC002802.

Keller, W., and J. Wright (1975), Microwave scattering and the straining of wind-generated waves, *Radio Sci.*, *10*(2), 139–147.

Kudryavtsev, V., D. Akimov, J. Johannessen, and B. Chapron (2005), On radar imaging of current features: 1. Model and comparison with observations, *J. Geophys. Res.*, *110*, C07016, doi:10.1029/2004JC002505.

Kudryavtsev, V., A. Myasoedov, B. Chapron, J. A. Johannessen, and F. Collard (2012a), Imaging mesoscale upper ocean dynamics using synthetic aperture radar and optical data, *J. Geophys. Res.*, *117*, C04029, doi:10.1029/2011JC007492.

Kudryavtsev, V., A. Myasoedov, B. Chapron, J. A. Johannessen, and F. Collard (2012b), Joint Sun-glitter and radar imagery of surface slicks, *Remote Sens. Environ.*, *120*, 123–132.

Longuet-Higgins, M. S. (1957), The statistical analysis of a random, moving surface, *Philos. Trans. R. Soc. London, Ser. A*, *249*(966), 321–387.

Lund, B., H. C. Graber, H. Tamura, C. Collins, and S. Varlamov (2015), A new technique for the retrieval of near-surface vertical current shear from marine X-band radar images, *J. Geophys. Res. Oceans*, *120*, 8466–8486, doi:10.1002/2015jc010961.

Lyzenga, D. R. (1998), Effects of intermediate-scale waves on radar signatures of ocean fronts and internal waves, *J. Geophys. Res.*, *103*(C9), 18,759–18,768.

McWilliams, J., F. Colas, and M. Molemaker (2009), Cold filamentary intensification and oceanic surface convergence lines, *Geophys. Res. Lett.*, *36*, L18602, doi:10.1029/2009GL039402.

Munk, W., L. Armi, K. Fischer, and F. Zachariasen (2000), Spirals on the sea, *Philos. Trans. R. Soc. London, Ser. A*, *456*, 1217–1280.

Phillips, O. M. (1984), On the response of short ocean wave components at a fixed wavenumber to ocean current variations, *J. Phys. Oceanogr.*, *14*, 1425–1433.

Plant, W. J. (1982), A relationship between wind stress and wave slope, *J. Geophys. Res.*, *87*, 1961–1967.

Rascle, N., B. Chapron, A. Ponte, F. Ardhuin, and P. Klein (2014), Surface roughness imaging of currents shows divergence and strain in the wind direction, *J. Phys. Oceanogr.*, *44*(8), 2153–2163.

Rascle, N., F. Nouguier, B. Chapron, A. Mouche, and A. Ponte (2016), Surface roughness changes by finescale current gradients: Properties at multiple azimuth view angles, *J. Phys. Oceanogr.*, *46*(12), 3681–3694.

Roullet, G., and P. Klein (2010), Cyclone-anticyclone asymmetry in geophysical turbulence, *Phys. Rev. Lett.*, *104*(21), 218501.

Salomonson, V. V., W. Barnes, P. W. Maymon, H. E. Montgomery, and H. Ostrow (1989), MODIS: Advanced facility instrument for studies of the Earth as a system, *IEEE Trans. Geosci. Remote Sens.*, *27*(2), 145–153.

Scully-Power, P., (1986), Navy oceanographer shuttle observations: STS 41-G mission report, *Tech. Rep. DTIC Doc.*, Naval Underwater Syst. Cent., Newport, R. I.

Shcherbina, A. Y., E. A. D'Asaro, C. M. Lee, J. M. Klymak, M. J. Molemaker, and J. C. McWilliams (2013), Statistics of vertical vorticity, divergence, and strain in a developed submesoscale turbulence field, *Geophys. Res. Lett.*, *40*, 4706–4711, doi:10.1002/grl.50919.

Thompson, D., and R. Gasparovic (1986), Intensity modulation in SAR images of internal waves, *Nature*, *320*, 345–348.

Yoder, J. A., S. G. Ackleson, R. T. Barber, P. Flament, and W. M. Balch (1994), A line in the sea, *Nature*, *371*(6499), 689–692.